Journal of Marine Research, 64, 249–266, 2006

Simulation and energy partition of the flow through Paso Galvarino, Chile

by Michael W. Stacey[1] and Arnoldo Valle-Levinson[2]

ABSTRACT

Paso Galvarino is a constriction in Seno Ventisquero, a tidally-energetic Chilean fjord. The pass is about 1500 m long and constricts in width by about 90 % near its sill, which has a depth of about 8 m. A laterally-averaged numerical model is compared to ADCP and backscatter observations of the hydraulic flow near the sill, during maximum flood, the slack tide after the flood, maximum ebb, and the slack tide after the ebb. The model is also used to examine how the energy flux into the fjord is partitioned in the region of the constriction. Energy is removed from the surface tide near the sill and is largely dissipated near the sill. The model predicts that the internal tide is unimportant and that energy transport by advection is much more important than that due to radiation. Advection is significant only near the sill, however, and a counteracting surface flux develops that suppresses the influence of the advection.

1. Introduction

Paso Galvarino is a narrow pass that connects the northern and southern portions of the fjord Seno Ventisquero (Fig. 1) in southern Chile. The pass is about 1500 m long and shallows to about 8 m depth. The fjord is about 2 km wide whereas the pass is only about 200 m wide, so the pass represents a very significant constriction along the length of the fjord.

The semi-diurnal tidal amplitude is estimated to be about 1 m and tidal currents in excess of 0.5 m/s have been measured in the pass with an Acoustic Doppler Current Profiler (ADCP) (Valle-Levinson *et al.*, 2001). While these observations were being made, there was a distinct surface layer about 5 m deep. The density increased from about 15 sigma-*t* at the pycnocline at about 5 m depth to about 24-26 sigma-*t* at 10-14 m depth. The rate of freshwater runoff into the fjord was estimated to be about 50 m^3/s (Valle-Levinson, personal communication).

Valle-Levinson *et al.* (2001) found that, because of the pass' small dimensions, the velocity field throughout the pass could be measured quasi-synoptically as it evolved over a tidal cycle. They found that they could interpret the flow within the context of two-layer

1. Department of Physics, Royal Military College of Canada, P.O. Box 17000, Station Forces, Kingston, Ontario, K7K 7B4, Canada. ***email: stacey-m@rmc.ca***

2. Department of Civil and Coastal Engineering, University of Florida, Gainesville, Florida, 32611, U.S.A.

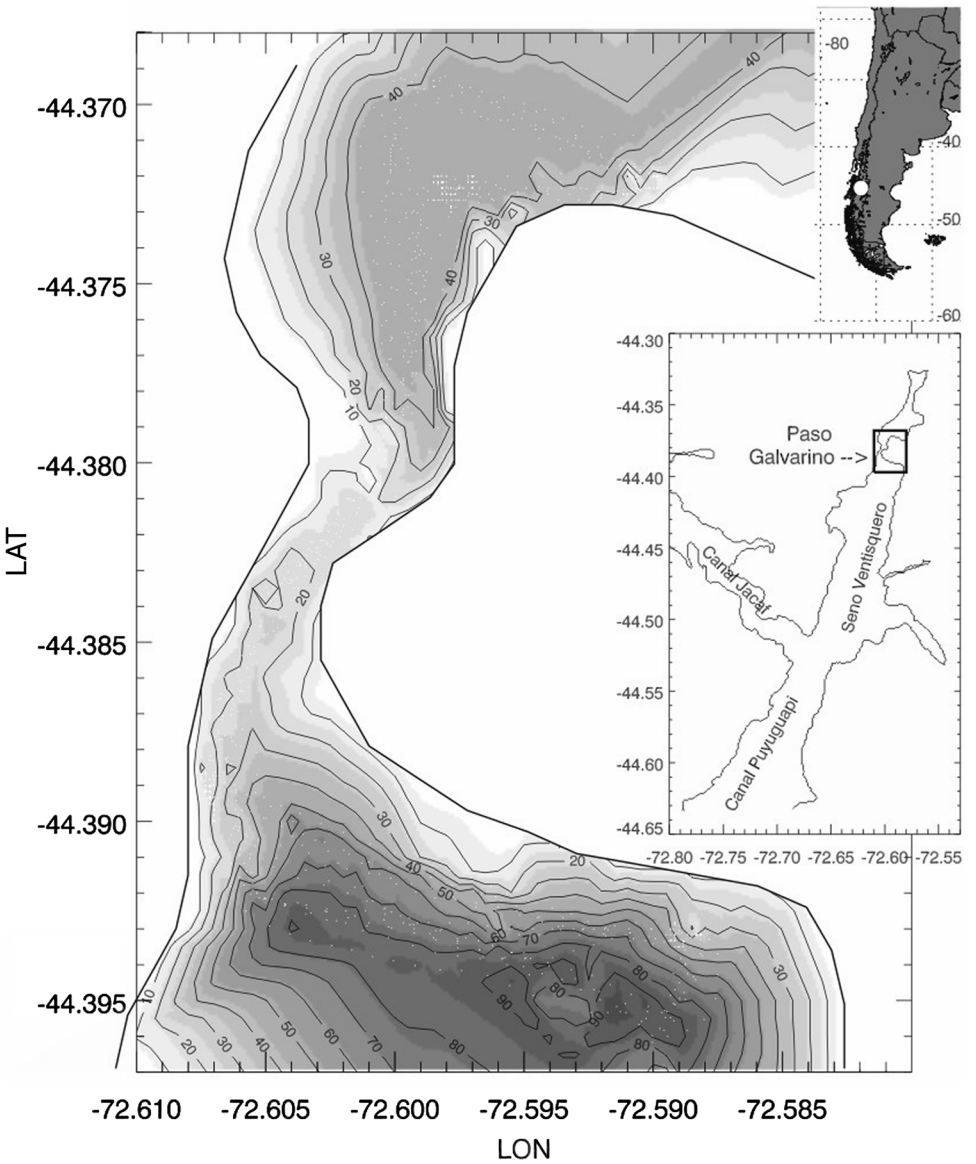

Figure 1. Area of study featuring Paso Galvarino. The upper right insert shows the region of South America (white circle) where the study took place. The middle right insert represents a detailed view of the fjords and inlets around Paso Galvarino. The bathymetry of Paso Galvarino is contoured every 10 m, from 0 to 90 m with solid contours. Shaded contours are presented at 10 m intervals from 5 to 95 m. White dots represent the location of ADCP flow and backscatter measurements.

hydraulic theory, and that when the barotropic flow direction changed, the slope of the pycnocline changed also.

The tides are a very important part of the circulation in the pass and are therefore a possible source of energy for mixing within the pass and within the fjord as a whole. Valle-Levinson *et al.* (2001) noted that vertical mixing in the pass 'can redistribute dissolved and suspended materials to and from the bottom of the pass with every tidal cycle.' Given the importance of the tides in the fjord, it is worthwhile to have an estimate of the net flux of tidal energy into the fjord and how this flux is partitioned. There are not enough observations to make this estimate, but such an estimate can be made with the help of a theoretical model. This has been done for a number of Canadian fjords [e.g., Observatory Inlet (Stacey, 1984); Knight Inlet (Stacey, 1985; Stacey and Pond, 1992); Saguenay Fjord (Stacey and Gratton, 2001)], and for the case of Knight Inlet in particular, there were sufficient observations to confirm the reliability of the models. Extensive observations of velocity, temperature and salinity in Knight Inlet (Webb and Pond, 1986; Baker and Pond, 1995) have shown that laterally-integrated models (Stacey and Pond, 1992; Stacey *et al.*, 1995) can simulate the tidally-forced circulation. The ability of the model of Stacey *et al*. (1995) to simulate the portion of the circulation forced by the winds and freshwater runoff has also been validated.

The Chilean fjord under consideration here is much smaller than Knight Inlet, and Knight Inlet does not have a width constriction at its sill. Therefore one might reasonably speculate that the partition of tidal energy within the two fjords is different. The internal tide has been found to be important in Knight Inlet and in other similar inlets. Given the geometry of Seno Ventisquero, however, it is quite possible that the tidal component of the circulation is not dominated by the internal tide. In fact, we will show that, according to the model, the simulated advective energy flux is larger than that of the internal tide in Seno Ventisquero.

Tinis (1995) and Tinis and Pond (2001) found that the internal tide was not important in Sechelt Inlet either. It is a fjord with a narrow constriction also, and energy was calculated to be removed from the barotropic (i.e., surface) tide at a rate of about 42 MW. Almost all of this energy was found to be dissipated in the immediate vicinity of the sill. The rate at which energy was removed from the surface tide was calculated using the expression

$$P \approx \rho g \frac{\eta_0^2 S \omega}{2} \frac{\sin(2\phi)}{2} \tag{1}$$

where ρ is the water density; g is the acceleration due to gravity; η_0 is the amplitude of the surface displacement of the tidal constituent; S is the surface area of the fjord, up-fjord of the sill; ω is the angular frequency of the tidal constituent; ϕ is the change in phase of the tidal height across the constriction. Tinis assumes that the surface height and phase change abruptly at the sill, and that on either side of the sill the amplitude and phase do not vary. Expression (1) was also derived, in a different manner and by making different assumptions, by Stigebrandt (1999). The validity of (1) for Seno Ventisquero will be tested by

comparing the energy flux of M_2 tidal energy in the fjord calculated from the numerical model to that determined from (1).

2. The model

The model will be the same as that used by Stacey *et al*. (1995), as modified by Stacey and Pond (1997) to account for the influence of surface waves on the near-surface circulation. The winds are not included in the simulation presented in this paper, and the modified and unmodified models produce essentially the same tidally-forced circulation. This model is laterally-averaged (i.e., two-dimensional) and hydrostatic, but it is nonlinear and includes the Mellor-Yamada level 2.5 turbulence closure scheme for determining the turbulent diffusion coefficients. The details of the model formulation can be found in Stacey *et al.* (1995) and Stacey and Pond (1997).

The vertical $\hat{z}$ coordinate in the model is related to the standard cartesian z coordinate (both taken to increase in the downward direction) via the transformation

$$\frac{\hat{z}}{H} = \frac{z + \eta}{D} \tag{2}$$

where $D(x,t) = H(x)+\eta(x,t)$ is the total water depth, $H(x)$ is the mean water depth, and $\eta(x,t)$ is the sea-surface displacement. Note that although $\hat{z} = H$ when $z = H$, $\hat{z} = 0$ when $z = -\eta$ so that the sea-surface in the (x, $\hat{z}$, t) space is always horizontal and motionless. Therefore, one can easily make the vertical resolution in the numerical model near the surface finer than the range of the tides, which is useful if the tidal range is significant. For Seno Ventisquero the tidal amplitude is about 1 m (so the range is about 2 m) and the shallowest depth in the pass is about 8 m, so a vertical resolution finer than the tidal range is obviously required.

Figure 2 shows the model grid. Note that the open boundary of the model is set far away from our region of interest which is the shallow region where the pass is located and for which there are ADCP observations. Given the geometry of the fjord, it may be that a realistic simulation of the circulation outside the pass will require a three-dimensional model. Within the narrow region of the pass itself however the two-dimensional model should be as applicable as it is to Knight Inlet, for example. The large region down-fjord of the pass is included in the model so that the open boundary can be placed far from the pass. Note that because the model is laterally-averaged, as opposed to width-independent [i.e., the width $B(x,\hat{z},t)$ is a function of depth and horizontal position], the constricting effect caused by the narrowing of the fjord in the region of the pass is taken into account. The widths as a function of horizontal position and depth within and just outside the pass were taken from Figure 1. Therefore, within our region of interest we have prescribed realistic model geometry. (The surface widths of the fjord throughout the model domain were taken from the lower insert of Figure 1.) At depth, outside the region of interest, the widths were

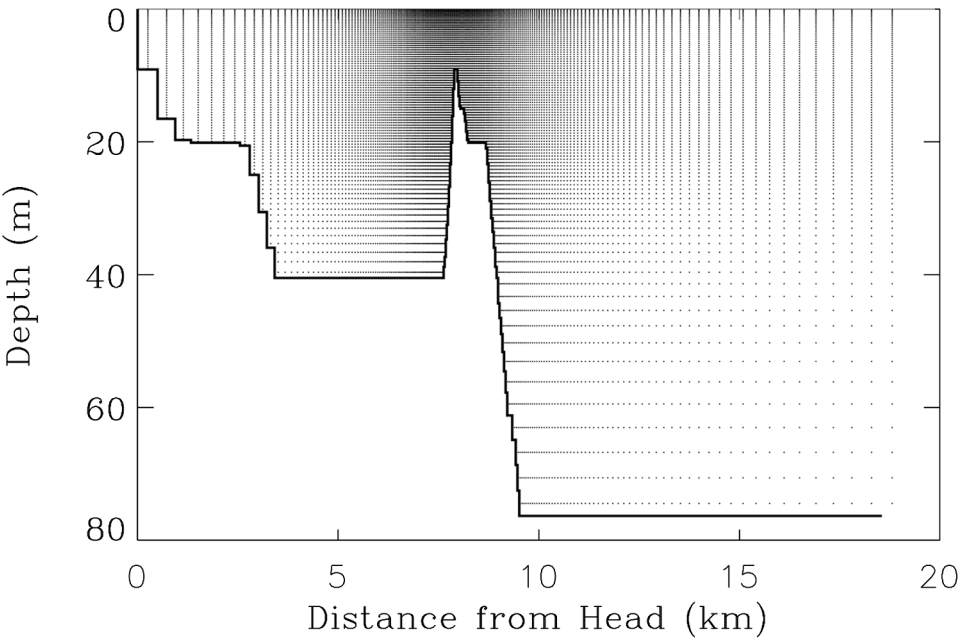

Figure 2. The model grid. Density grid points are shown.

chosen to vary in a smooth fashion, and they were made to meld smoothly with the widths at depth in the region of interest obtained from Figure 1. We will not be discussing the circulation outside our region of interest.

The initial density field of the model is horizontally homogeneous and is based on measurements made in the pass down to a depth of 14 m (Fig. 2a, b of Valle-Levinson *et al*., 2001). It is10 sigma-*t* from the surface down to 3 m, and then increases to 15 sigma-*t* at 5 m, the location of the pycnocline. It increases to 24 sigma-*t* at 14 m. Below 14 m, the initial density is prescribed to increase to 26 sigma-*t* at 40 m, and 28 sigma-*t* at 60 m. Below 60 m it remains at 28 sigma-*t*.

Tidal forcing is imposed in the model by prescribing the surface height at the open boundary. Here, we force at only the M_2 frequency (period = 12.42 hrs) with an amplitude of 1 m. Freshwater runoff at the head of the fjord is set at 50 m^3/s. The winds are set to zero.

All adjustable parameters, such as the drag coefficient (=0.003) and the background mixing, are the same as in Stacey *et al*. (1995). Until more observations are available from Seno Ventisquero it makes little sense to adjust them. The value used for the drag coefficient is well within the limits set for it in many flow regimes, and the background mixing is only important outside the pass and well outside the region of interest.

The model was run for a simulation time of 15 days. This is long enough so that harmonic analysis can give reasonable estimates of M_2 amplitude and phase.

3. The energy balance

In (x, $\hat{z}$, t) space the sectionally-integrated, time-averaged energy fluxes can be expressed as (Stacey and Gratton, 2001):

$$\overline{\int_0^H B\tilde{d}\rho_0 g u \eta d\hat{z}} \tag{3a}$$

$$\overline{\int_0^H B\tilde{d} u p d\hat{z}} \tag{3b}$$

$$\overline{\int_0^H B\tilde{d}\rho_0 \frac{u^2}{2} u d\hat{z}} \tag{3c}$$

$$\overline{-\int_0^H B\tilde{d}\rho_0 A_H \frac{\partial}{\partial x}\left(\frac{u^2}{2}\right) dz} \tag{3d}$$

where

$$p = \int_0^{\hat{z}} \tilde{d} g \rho' d\hat{z} = \tilde{d}\tilde{p} \tag{4}$$

and

$$\tilde{d} = \frac{H + \eta}{H}\,. \tag{5}$$

The density $\rho = \rho_0 + \rho'$ where ρ_0 is a constant reference density ($\approx 10^3 \mathrm{kg/m}^3$) and ρ' is related to all variations, including the depth variation in the mean density profile. The term g is the acceleration due to gravity; A_H (x,$\hat{z}$,t) is the horizontal eddy viscosity, and u(x,$\hat{z}$,t) is the along-channel component of the velocity.

The energy flux due to the total pressure ($\rho_0 g\eta + p$) is given by (3a,b) together, and the advective and diffusive fluxes are given by (3c) and (3d) respectively. The term (3a) gives the energy flux due to variations in the surface displacement $\eta(x,t)$ and the total horizontal velocity $u(x,z,t)$, and (3b) gives the energy flux due to the pressure $p(x,z,t)$ caused by variations in the density field and the total horizontal velocity, given that the reference density has been chosen to be ρ_0. Values for the flux as given by (3a) are not sensitive to any reasonable choice of ρ_0 since the density varies by only a few percent in the ocean. However, small variations in the choice of ρ_0 can cause significant variations in the flux as given by (3b). In the overall mechanical energy balance, the horizontal divergence of these

variations can be compensated by variations in the rate of change of potential energy (Stacey and Gratton, 2001).

For the simulation presented here, the total surface, advective and diffusive energy fluxes will be plotted, as a function of horizontal distance from the head of the inlet system, as they are given above (3a, c and d). So, the advective and diffusive energy fluxes due to the total flow will be presented as well as that for the total surface displacement relative to mean sea-level. The term (3a) does not give the energy flux due to the barotropic tide as it is commonly defined because other processes (e.g., the internal tide and advection) can influence the surface layer, and typically only the depth-averaged velocity (transport) would be used when calculating the energy flux due to the barotropic tide. However, it will be shown that the internal tide is not very energetic relative to the total energy flux, so its influence on the total flux is small. Advection, however, has an influence on the surface layer.

The energy flux due to the internal and barotropic tides will be calculated by harmonically analyzing the density, surface displacement and horizontal velocity fields for the M_2 component of those fields. Then the M_2 component of the total pressure and horizontal velocity fields are separated into a mean over depth and a fluctuation such that

$$\rho_0 g \eta_0 + \tilde{p}_0 = \langle p_0 \rangle + p_0'$$
$$u_0 = \langle u_0 \rangle + u_0'$$

where

$$\int_0^H p_0' d\hat{z} = 0 \tag{6}$$

$$\int_0^H B_0 u_0' d\hat{z} = 0.$$

(The $< >$ represents the depth-average.) Here, we are taking u_0, η_0 and $\tilde{p}_0$ to be the M_2 components of the horizontal velocity, surface displacement, and from (4) the pressure. (The term $B_0(x,\hat{z})$ is the fjord width, for which the slight dependence on time, included in $B(x,\hat{z},t)$ in (3), has been removed.) The sectionally-integrated energy fluxes, averaged over a tidal cycle, due to the barotropic and internal tides are then (respectively)

$$\overline{\int_0^H B_0 \langle p_0 \rangle \langle u_0 \rangle d\hat{z}} \tag{7}$$

$$\overline{\int_0^H B_0 p_0' u_0' d\hat{z}}. \tag{8}$$

The overbars represent a time-average, which is easily calculated when only a single tidal constituent is considered.

4. Results

a. Velocity and density fields

The observations reported by Valle-Levinson *et al*. (2001) in Paso Galvarino throughout one tidal cycle showed that the pycnocline sloped in different directions from flood to ebb flows. During flood, it sloped downward on the upstream (northern) side of the sill and during ebb it sloped downward on the downstream (southward) side of the sill (Fig. 3). The direction of the slope was consistent with the sense of the tidal flow and followed theoretical considerations related to unidirectional stratified flow over a sill or contraction (Baines, 1995). The vertical excursions of the pycnocline and the horizontal extent of vertical mixing were asymmetric on either side of the pass. Vertical excursions of the pycnocline were greater on the southern end of the pass during ebb than on the northern end during flood because of greater instabilities on the pycnocline produced by ebb flows interacting with the pass. Also, the horizontal extent of vertical mixing was longer during ebb than during flood because the distance between the point of mixing initiation (thought to be the hydraulic control point) and the end of the pass is greater in the ebb than in the flood direction (Fig. 3).

Tidal currents within the pass typically increased from < 20 cm/s to > 50 cm/s and then decreased dramatically past the pass (Fig. 3). Within the pass, the currents became strong enough to produce unidirectional (nearly depth-independent) flow during periods around maximum ebb and flood flows. Changes in pycnocline depth associated with flow accelerations and decelerations along the pass were consistent with expected hydraulic behavior in terms of a composite Froude number (e.g. Farmer and Armi, 1999; Valle-Levinson *et al.*, 2001). During the early stages of flood or ebb the flow was subcritical along the pass and the pycnocline was practically unperturbed by the flow along the pass. At around maximum flood, however, the flow accelerated greatly inside the pass and then rapidly decelerated. These sharp transitions from subcritical to supercritical flow and back to subcritical were reflected by vertical excursions of the pycnocline and the presence of a leeward internal hydraulic jump (Fig. 3a, b). At around maximum ebb, the pycncoline bulged up just upstream (relative to the tidal flow direction) of the narrowest section of the pass, right before the transition from subcritical to supercritical flow. Once again, the transition from supercritical to subcritical flow resulted in an internal hydraulic jump leeward of the section (Fig. 3e, f). These hydraulic jumps that develop around maximum tidal currents suggested large energy transformations from mixing processes that occurred at the pass.

To compare the simulation to the observations, we have picked a time interval starting with a maximum flood about six days into the simulation. Model velocity and sigma-*t* were stored at simulated time intervals of one hour. Therefore, the time picked for comparison

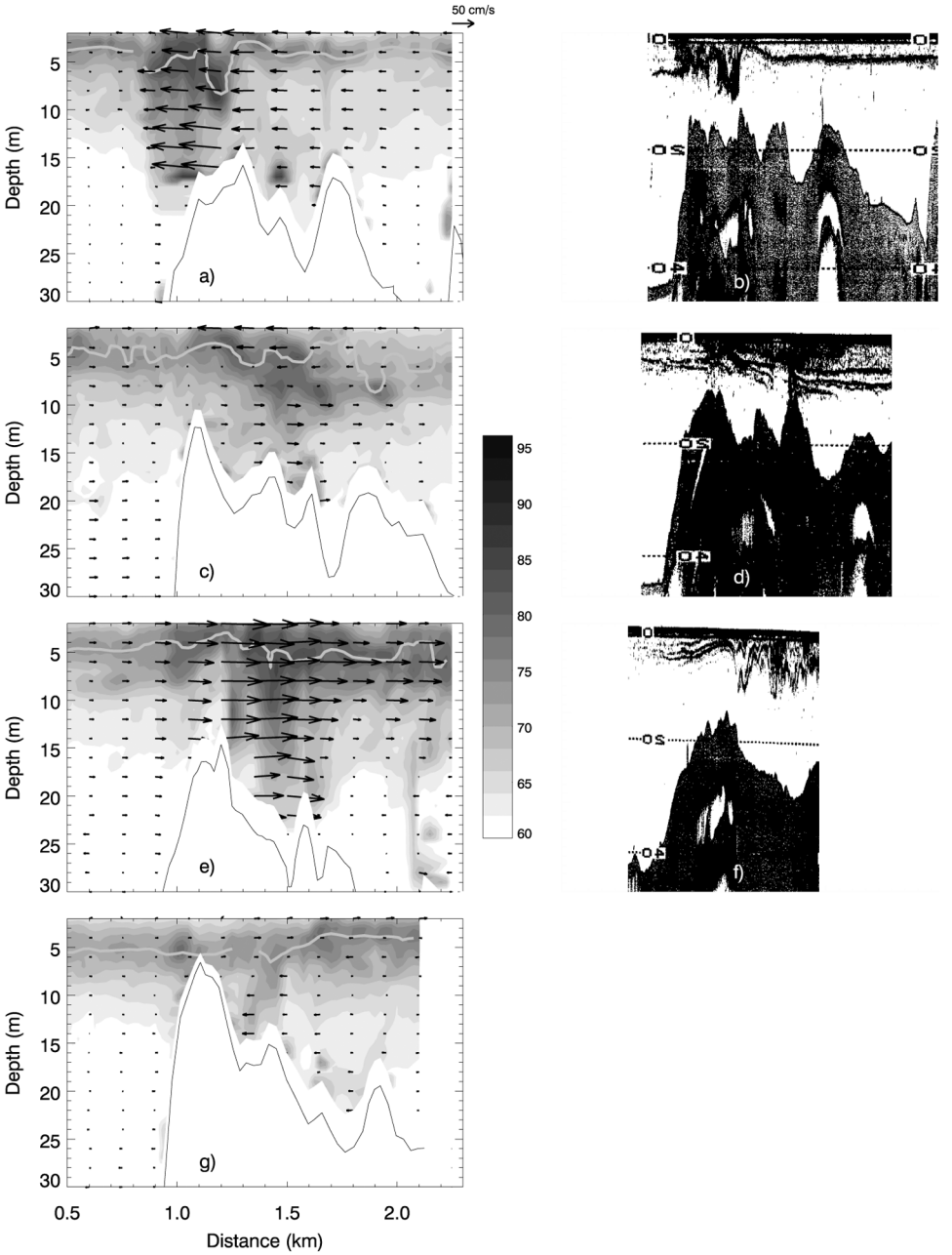

Figure 3. Along-fjord sections of (a, c, e, g) ADCP flow and backscatter fields, and (b, d, f) echo sounder backscatter. The upper-most row represents maximum flood conditions, the next row shows end of flood, then maximum ebb, and the lowest row portrays end of ebb conditions. North (toward the head of the fjord) is to the left, and south (toward the mouth of the fjord) is to the right. Here flow is represented by vectors and ADCP backscatter by shaded contours at intervals of 5 decibels. Flow and backscatter scales are given to the right. Maximum backscatter positions along the pass are denoted by the thick, gray line that resembles the echo sounder trace. Flow vectors are shown every 2 m in the vertical and every 150 m in the horizontal. The bottom profile is shown as the black continuous line. The area of hampered quality in the velocity data (owing to ADCP side lobe effects) is masked in white just above the bottom profile.

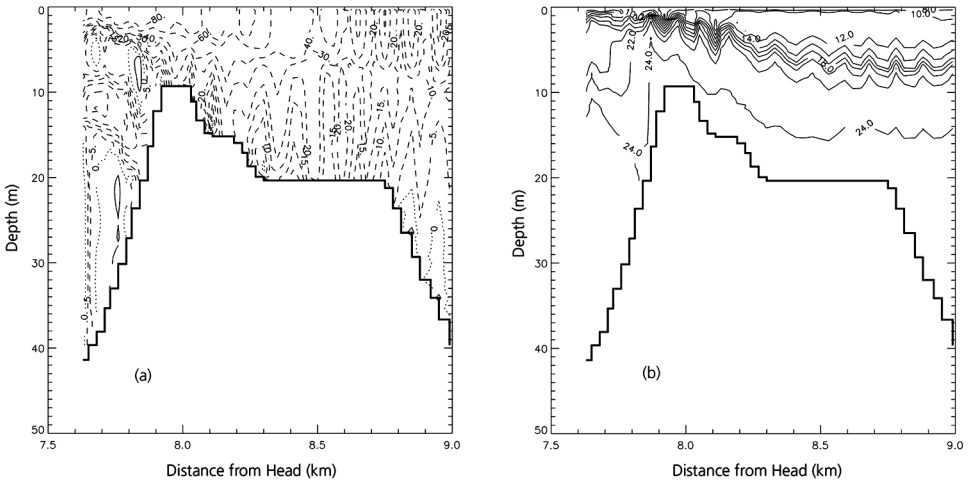

Figure 4. The along-channel velocity (a) and sigma-*t* (b) near maximum flood tide. In (a) the dashed lines signify flow (cm/s) from right to left (towards the head), and the solid lines signify flow from left to right (towards the mouth). The dotted lines are zero contours.

with the data was a time close to, but not exactly at, the time of maximum flood. The same goes for the contours at other stages of the tide also. Four sets of figures (Figs. 4 to 7) show the simulated velocity and sigma-*t* at maximum flood (Fig. 4), the slack tide following the flood (Fig. 5), the following maximum ebb (Fig. 6), and the slack tide following the ebb (Fig. 7). The time interval between contour plots is three hours.

The simulated contours can change significantly over time. Also, the model is laterally-averaged and therefore cannot take into account the lateral variations that are evident in the

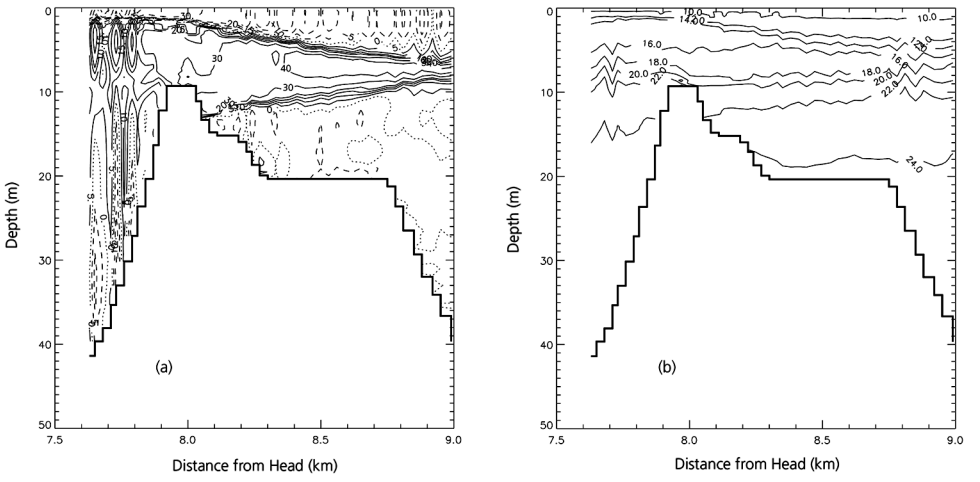

Figure 5. As for Figure 4, but 3 hours later, during slack tide after the flood.

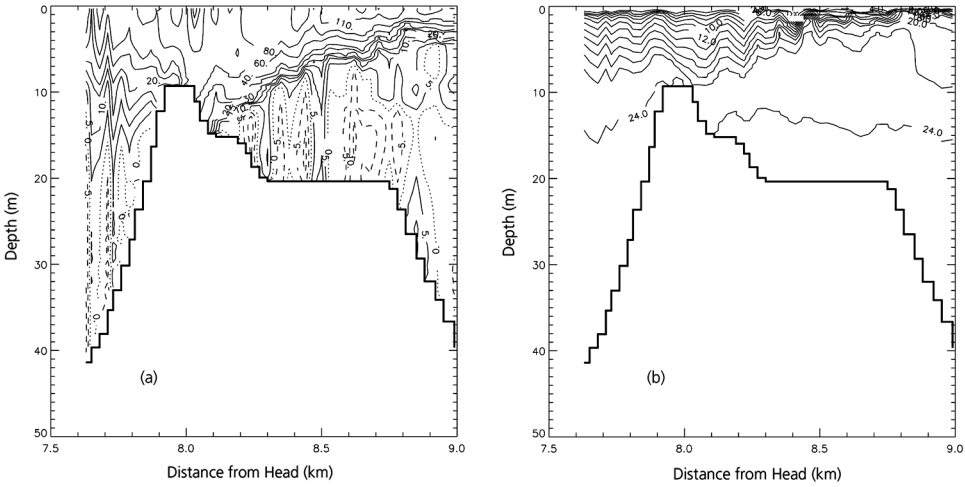

Figure 6. As for Figure 4, but 6 hours later, during maximum ebb.

bottom topography. (See Figs. 3 a, c, e, and g and how the bottom topography varies for each transect). So a detailed comparison between the simulation and the observations has not been made, and no effort has been made to make sure that the state of the tide for the simulation corresponds precisely to that of the observations.

During the flood the simulated flow is unidirectional, as it is in the observations (Fig. 3a) and speeds greater than 50 cm/s over the shallowest part of the pass are certainly achieved. On the lee (i.e., down-flow) of the sill, the speeds decrease dramatically at 15-20 m depth. There is also a hydraulic jump (Fig. 4b) on the lee of the sill.

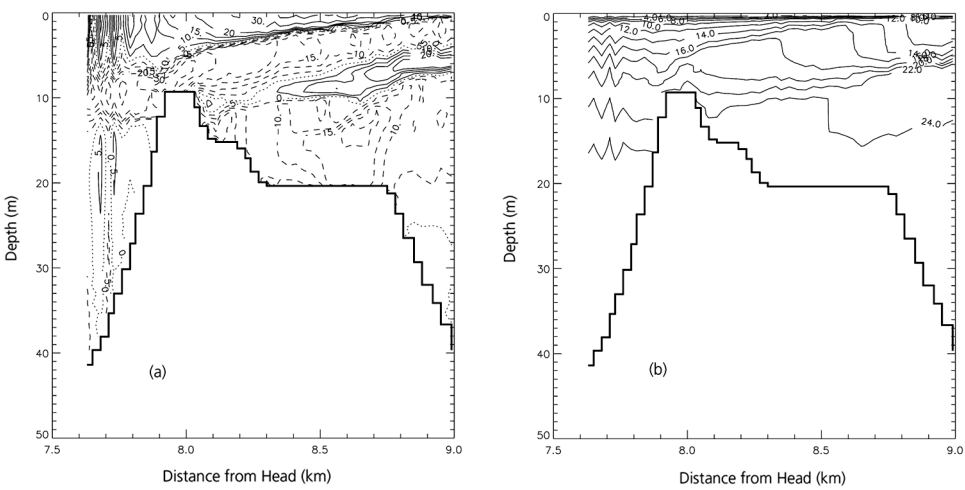

Figure 7. As for Figure 4, but 9 hours later, during slack tide after the ebb.

During the following slack tide, the flow is inward (to the left in Fig. 5a) near the surface and outward (to the right in Fig. 5a) below. Underneath the outward flow and down-flow from the sill, there is a region where the velocity is very small in magnitude. These characteristics are also observed (Fig. 3c). The isopycnals (Fig. 5b) are relatively undisturbed, and deeper than during maximum flood (Figs. 4b and 5b), in agreement with the observations (Figs. 3b and d).

During the ebb tide, the flow is unidirectional in the immediate region of the sill (Fig. 6a), but farther down-flow there is a region extending to the bottom where the magnitude of the velocity is very small. This characteristic is in agreement with the observations (Fig. 3e). The isopycnals (Fig. 6b) show hydraulic transition where the pass becomes deeper than 20 m, but no lee wave (or hydraulic transition) closer to the sill. Earlier in the ebb (contours not shown), there is some indication of hydraulic transition in the lee of the sill, but it is subsequently swept down-flow. Because the model is hydrostatic, it could not simulate any down-flow lee waves because they are associated with nonhydrostatic processes.

During the following slack tide, at the end of ebb, the flow (Fig. 7a) tends to be outward at the top and inward at the bottom, in agreement with the observations (Fig. 3g). In the simulations, down-flow of the sill there is a mid-depth region with very small flow followed by outward flow. In the observations there is very small flow near mid-depth, but no evidence of outward flow. The isopycnals (Fig. 7b) show that the hydraulic transition is migrating closer to the sill in response to the smaller current speeds. No echo sounder trace is available for comparison at this time.

The correspondence between the observations and the simulation is sufficiently good to expect that calculations of the energy partition in the Pass will be realistic.

b. Energy fluxes

Figure 8 shows the amplitude and phase of the M_2 surface height, obtained by harmonic analysis. One sees clearly that there is a strong interaction of the sea surface with the constriction. Overall, the phase changes by about 1.5^0 across the constriction, and the amplitude exhibits noticeable variability also. Judging by the phase change, virtually all of the energy removal from the barotropic tide occurs at the constriction. From (1), using an amplitude of 1 m, a phase change ϕ of 1.5^0, a surface area up-fjord of the constriction of $S = 10^7$ m^2, and the angular frequency for the M_2 tide ($\omega = 1.4\times10^{-4}$ s^{-1}), one obtains 0.18 MW as the rate at which energy is removed from the M_2 surface tide. This is a small value compared to that obtained for other fjords (e.g., it can be over 10 MW for Observatory and Knight Inlets, and for the Saguenay Fjord) but Seno Ventisquero is significantly smaller than these other fjords. The phase change across the constriction is actually quite large. Note also that there is some small spatial scale variability in the phase, of up to about 0.2^0, on either side of where the phase changes abruptly. It is primarily numerical scatter here, although in some fjords (e.g., Knight Inlet) a phase change of 0.2^0 would not be insignificant.

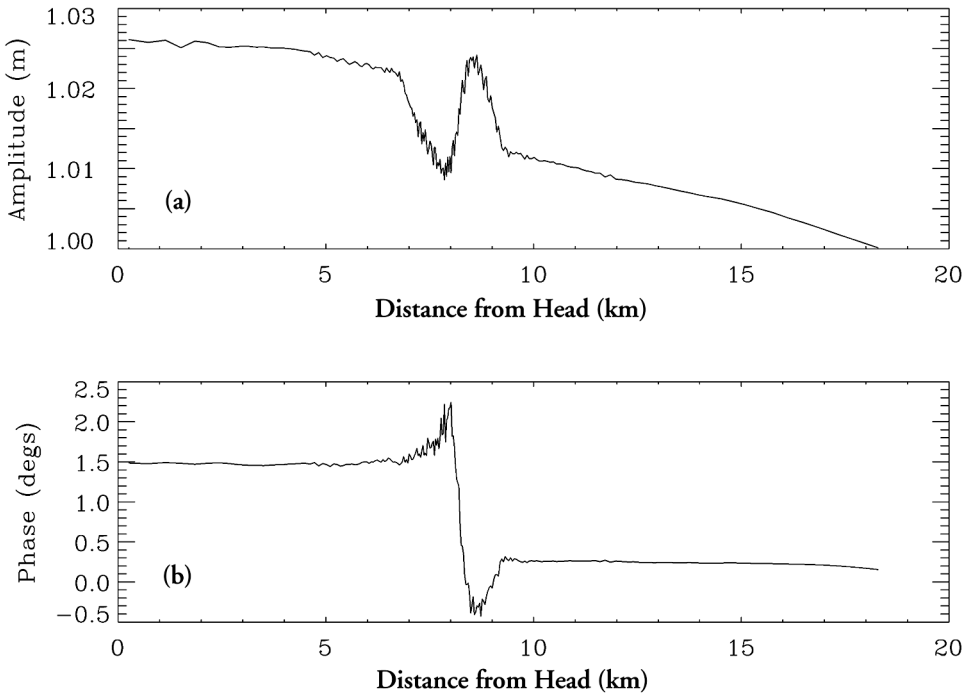

Figure 8. The amplitude (a) and phase (b) of the M_2 tidal height along the fjord.

Figure 9 shows the energy fluxes for (a) the surface displacement [using expression (3a)], (b) the internal tide [using expression (8)], (c) advection [using expression (3c)] and (d) diffusion [using expression (3d)]. Because of small scale variability, primarily in the surface displacement (see Fig. 8), there is considerable scatter in the energy flux due to the surface displacement, so when presenting it in Figure 9a it has been spatially averaged with a three-point moving average. This average removes noise on either side of where the flux near the constriction changes abruptly.

The up-fjord energy flux due to the surface displacement (Fig. 9a), at 9-10 km from the head, where the fjord suddenly shallows and the constriction occurs (see Figs. 1 and 2), is about 0.15-0.2 MW, close to the value calculated using expression (1). Note that the phase in the tidal surface height (Fig. 8b) and the energy flux due to the surface displacement (Fig. 9a) change abruptly at about the same distance from the head.

The energy flux due to the internal tide is shown in Figure 9b. This flux is significantly less than the net flux into the fjord due to the surface displacement (Fig. 9a). The largest flux due to the internal tide (about -0.04 MW) is an up-fjord flux about 8-9 km from the head, where the fjord begins to constrict. The fluxes on either side of the constriction (less than about 7 km and more than about 10 km from the head) are directed away from the constriction.

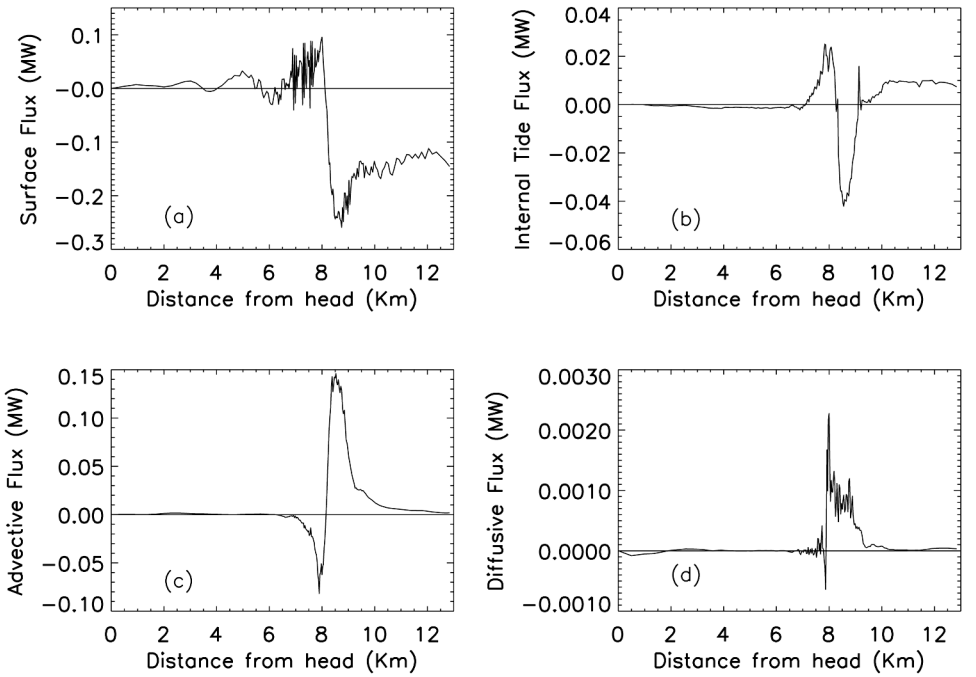

Figure 9. Energy flux along the fjord due to (a) the surface displacement [expression (3a)], (b) the internal tide [expression (8)], (c) advection [expression (3c)], and (d) diffusion [expression (3d)].

Figure 9c shows the advective energy flux. This flux is larger than that due to the internal tide (Fig. 9b), and it tends to transport energy away from the constriction. The fluxes are significant only near the constriction, however; advection does not transport significant energy out of the pass in either direction. Nevertheless, it is locally very important.

Figure 9d shows the diffusive energy flux. It does not make an important contribution to the total flux balance.

Between 7.5 and 8.5 km from the head (which includes our primary region of interest; see Fig. 4 for example) the simulated, time-averaged, total dissipation rate is about 0.20 MW. There is a total net energy flux due to the surface displacement (Fig. 9a) into the region of 0.34 MW, and a total net advective flux out of the region (Fig. 9c) of 0.16 MW. So, the sum of the total net energy fluxes due to advection and the surface displacement (0.18 MW into the region) differs from the dissipation rate by only 0.02 MW. (Some, but not all, of this difference will be due to numerical uncertainty.) There is a net energy flux into the region due to the internal tide (Fig. 9b) of about 0.05 MW. The rate of change of the kinetic energy in this region was very small ($\approx 10^{-5}$ MW), which leaves, therefore, about 0.03 MW for the rate of increase in the potential energy. The main energy balance is between the dissipation rate and the net energy fluxes into the region due to the surface displacement and the advection.

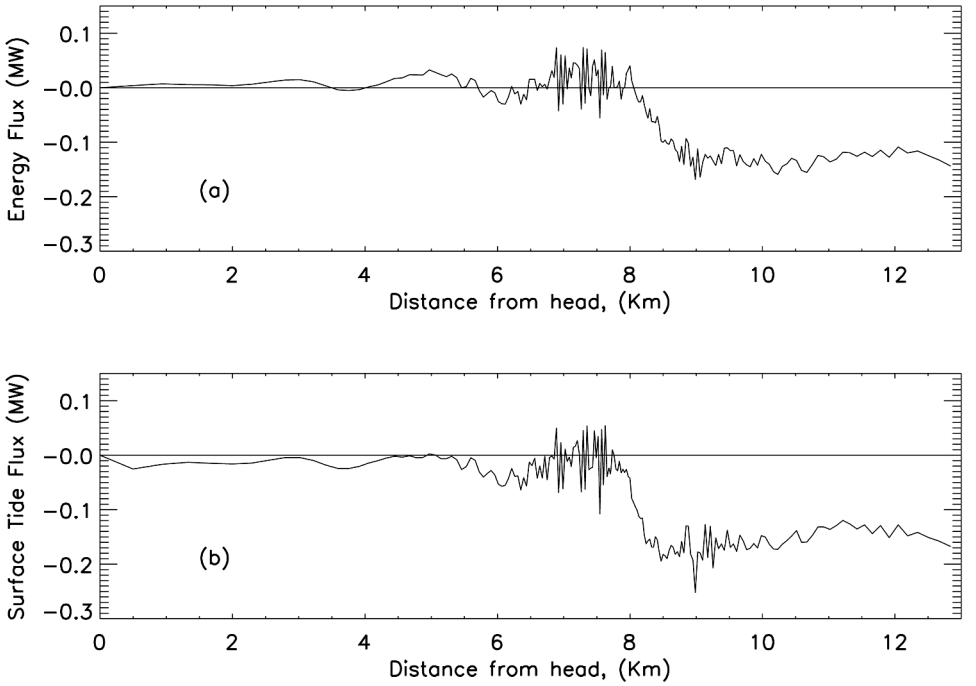

Figure 10. Energy flux along the fjord due to (a) the sum of expressions (3a) and (3c) [i.e., the sum of the total energy flux due to the surface displacement and total advection], and (b) the surface tide [expression (7)].

The energy flux due to the surface displacement as plotted in Figure 9a includes all processes that may influence the surface displacement. That is, it is not necessarily a measure of the flux due to the barotropic tide alone. Stacey and Pond (2005) showed that for Knight Inlet this surface energy flux can be significantly different than the flux due to the barotropic tide alone. For the case of Knight Inlet, the internal tide is quite important. For the case of Paso Galvarino, advection is more important and it influences the total energy flux due to the surface displacement. Figure 10a shows the sum of the energy fluxes due to the surface displacement (Fig. 9a) and advection (Fig. 9c). Figure 10b shows the energy flux due to the barotropic tide [using expression (7)]. (Figure 10b has been spatially averaged, as was Figure 9a, to remove numerical noise.) Note that the two flux plots are similar and that the major feature in both is the abrupt change in the energy flux near the constriction. The similarity between theses two flux plots suggests that major influences on the total energy flux due to the surface displacement are the advective flux and the energy flux due to the barotropic tide. The surface displacement develops an ‘extra’ energy flux near the constriction that counterbalances the advective flux. Since this ‘extra’ surface flux and the advective flux effectively cancel each other out, the main energetic balance can be

considered to be between the net barotropic tidal flux into the region near the constriction and the total dissipation rate near the constriction.

The dissipation rate has four components (e.g., Stacey and Gratton, 2001), representing the dissipation rates due to the bottom and sidewall stress and due to the vertical and horizontal diffusion of momentum. Bottom and sidewall stress account for 0.01 MW and 0.03 MW respectively, and vertical and horizontal diffusion account for 0.02 and 0.14 MW respectively. Therefore, according to the model most of the dissipation occurs because of horizontal variations in the flow field, which is perhaps not surprising since there is strong horizontal variability in the flow field near the constriction because the cross-sectional area of the fjord changes so much there. Because the model is laterally-averaged and has other limitations however, one should not conclude too much from this. A three-dimensional model might show the along-fjord variations to be less important.

Note that the net barotropic tidal flux into the region of the constriction is close to the dissipation rate in the region of 0.2 MW. Note also that this is close to the rate at which energy is removed from the barotropic tide according to expression (1). In applying (1), the phase change across the constriction was estimated to be 1.5^0 (see Fig. 8), by ignoring the noticeable fluctuation in phase near the constriction. [Note that this fluctuation has similarities to that of the surface energy flux (see Fig. 9a).] If the fluctuation in phase near the constriction were not ignored, the phase change would be about 2.5^0 and the energy flux calculated using (1) would be too large. However, this fluctuation is easily identified and can be accounted for. Expression (1), when applied to this situation, gives a good estimate of the rate at which energy is removed from the barotropic tide, as long as the fluctuation is discounted when determining the phase change across the constriction. For Knight Inlet (Stacey and Pond, 2005), the phase of the tidal surface height varies gradually along the inlet (it does not change abruptly at the sill where the energy is removed from the barotropic tide) and therefore application of an expression like (1) becomes more problematic.

5. Summary and conclusions

A laterally-integrated two-dimensional numerical model can simulate with reasonable accuracy the tidally-forced component of the circulation near the sill of Seno Ventisquero.

The rate at which energy is transported away from the constriction by the internal tide is very small compared to the rate at which energy is dissipated near the constriction. More energy is advected than is transported by the internal tide, but advection is important only near the constriction. Diffusion does not make an important contribution to the total energy flux in the fjord.

The total rate of energy dissipation near the constriction is balanced primarily by the net energy fluxes into the region due to (1) the total surface displacement (relative to mean sea level) and total horizontal velocity [expression (3a)], and (2) the total advection [expression (3c)]. The energy flux due to the barotropic tide [expression (7)] is similar to the sum

of expressions (3a) and (3c). That is, the total surface energy flux is composed of the flux due to the barotropic tide and a flux that counteracts the total advective flux. Therefore, one can consider the dissipation rate near the constriction to be balanced primarily by the net energy flux into the region due to the barotropic tide. According to the model, both the dissipation rate and the change in the energy flux due to the barotropic tide near the constriction is about 0.2 MW.

According to the model, the expression (1) (Tinis, 1995; Stigebrandt, 1999; Tinis and Pond, 2001) gives a reasonable estimate of the rate at which energy is removed from the surface tide near a constriction, for a flow where the phase in the surface height undergoes a sudden change near the constriction. The modeled phase change of about 1.5^0 across the constriction of Seno Ventisquero should be easily measurable. This phase measurement should be made well away from either side of the constriction, to avoid fluctuations in the phase that may occur near the constriction.

Acknowledgments. The assistance of R. C. Kidd, C. Molinet, F. Jara and D. Soto during data collection is gratefully acknowledged. Mr. Terry Hutchinson helped with the production of a number of the figures. AVL acknowledges support from NSF grant no. 9983685. We thank the reviewers for their helpful comments.

REFERENCES

Baines, P. G. 1995. Topographic Effects in Stratified Flows, Cambridge Univ. Press, 482 pp.

Baker, P. D. and S. Pond. 1995. Low frequency residual circulation in Knight Inlet, British Columbia, Canada. J. Phys. Oceanogr., *25*, 747-763.

Farmer, D. M. and L. Armi. 1999. The generation and trapping of solitary waves over topography. Science, *283*, 188-190.

Stacey, M. W. 1984. The interaction of tides with the sill of a tidally energetic inlet. J. Phys. Oceanogr., *14*, 1105-1117.

——1985. Some aspects of the internal tide in Knight Inlet, British Columbia. J. Phys. Oceanogr., *15*, 1652-1661.

Stacey, M. W. and Y. Gratton. 2001. The energetics and tidally-induced reverse renewal in a two-silled fjord. J. Phys. Oceanogr., *31*, 1599-1615.

Stacey, M. W. and S. Pond. 1992. A numerical model of the internal tide in Knight Inlet, British Columbia. Atmos. Ocean., *30*, 383-418.

——1997. On the Mellor-Yamada turbulence closure scheme: the surface boundary condition for q^2. J. Phys. Oceanogr., *27*, 2081-2086.

——2005. Energy fluxes due to the surface and internal tides in Knight Inlet, British Columbia. J. Phys. Oceanogr., *35*, 2219-2227.

Stacey, M. W., S. Pond and Z. P. Nowak. 1995. A numerical model of the circulation in Knight Inlet, British Columbia, Canada. J. Phys. Oceanogr., *25*, 1037-1062.

Stigebrandt, A. 1999. Resistance to barotropic tidal flow in straits by barotropic wave drag. J. Phys. Oceanogr., *29*, 191-197.

Tinis, S. W. 1995. The circulation and energetics of the Sechelt Inlet System, British Columbia. Ph.D. Thesis, University of British Columbia, 173 pp.

Tinis, S. W. and S. Pond. 2001. Tidal energy dissipation at the sill of Sechelt Inlet, British Columbia. J. Phys. Oceanogr., *31*, 3365-3373.

Valle-Levinson, A., F. Jara, C. Molinet and D. Soto. 2001. Observations of intratidal variability of flows over a sill/contraction in a Chilean Fjord. J. Geophys. Res., *106*, 7051-7064.

Webb, A. J. and S. Pond. 1986. A modal decomposition of the internal tide in a deep, strongly stratified inlet: Knight Inlet, British Columbia. J. Geophys. Res., *91*, 9721-9738.

Received: *22 April, 2004*; revised: *25 November*, *2005*.